Non-blind and Blind Deconvolution Under Poisson Noise Using Fractional-Order Total Variation

Mujibur Rahman Chowdhury, Jing Qin & Yifei Lou

ONLINE FIRST

Journal of Mathematical Imaging and Vision

ISSN 0924-9907

J Math Imaging Vis
DOI 10.1007/s10851-020-00987-0

Springer

Your article is protected by copyright and all rights are held exclusively by Springer Science+Business Media, LLC, part of Springer Nature. This e-offprint is for personal use only and shall not be self-archived in electronic repositories. If you wish to self-archive your article, please use the accepted manuscript version for posting on your own website. You may further deposit the accepted manuscript version in any repository, provided it is only made publicly available 12 months after official publication or later and provided acknowledgement is given to the original source of publication and a link is inserted to the published article on Springer's website. The link must be accompanied by the following text: "The final publication is available at link.springer.com”.

Springer

Author's personal copy

Journal of Mathematical Imaging and Vision
https://doi.org/10.1007/s10851-020-00987-0

Non-blind and Blind Deconvolution Under Poisson Noise Using Fractional-Order Total Variation

Mujibur Rahman Chowdhury[1] · **Jing Qin**[2] · **Yifei Lou**[1]

Received: 7 April 2020 / Accepted: 7 August 2020
© Springer Science+Business Media, LLC, part of Springer Nature 2020

Abstract

In a wide range of applications such as astronomy, biology, and medical imaging, acquired data are usually corrupted by Poisson noise and blurring artifacts. Poisson noise often occurs when photon counting is involved in such imaging modalities as X-ray, positron emission tomography, and fluorescence microscopy. Meanwhile, blurring is also inevitable due to the physical mechanism of an imaging system, which can be modeled as a convolution of the image with a point spread function. In this paper, we consider both non-blind and blind image deblurring models that deal with Poisson noise. In the pursuit of high-order smoothness of a restored image, we propose a fractional-order total variation regularization to remove the blur and Poisson noise simultaneously. We develop two efficient algorithms based on the alternating direction method of multipliers, while an expectation-maximization algorithm is adopted only in the blind case. A variety of numerical experiments have demonstrated that the proposed algorithms can efficiently reconstruct piecewise smooth images degraded by Poisson noise and various types of blurring, including Gaussian and motion blurs. Specifically for blind image deblurring, we obtain significant improvements over the state of the art.

Keywords Blind deconvolution · Poisson noise · Expectation-maximization · Fractional-order total variation

Mathematics Subject Classification 65F22 · 68U10 · 52A41 · 49N45

1 Introduction

Data acquired by any imaging sensor usually undergo many types of degradations, in which two prominent ones are noise and blur. Specifically in photon-counting systems, such as X-ray, positron emission tomography (PET), single-photon emission computerized tomography (SPECT), fluorescence microscopy, and telescope, Poisson distribution is more appropriate to describe the noise statistics than the standard Gaussian distribution. Moreover, the recorded images are typically blurry due to the physical mechanism of an imaging device. The blurring process can be characterized by a *point spread function* (PSF), which is an impulse response of the imaging system to a point source. For a linear shift-invariant (LSI) system, blurring can be mathematically described by a convolution of a clean image with a PSF, where the PSF serves as a blurring kernel (also known as convolution kernel). Therefore, image deblurring is often referred to as image deconvolution. In this paper, we focus on LSI systems and use the terms "deblurring" and "deconvolution" interchangeably. If the PSF is known a priori, then recovering a clean image from a blurry and noisy input is called *non-blind deconvolution*. If the PSF is completely unknown, then the problem becomes *blind deconvolution*.

1.1 Related Works

Both non-blind and blind deconvolutions are highly ill-posed inverse problems. A large number of deconvolution meth-

---

Qin is supported by the NSF DMS-1941197. Lou acknowledges the NSF CAREER award DMS-1846690.

✉ Yifei Lou
Yifei.Lou@utdallas.edu

Mujibur Rahman Chowdhury
mujib.chowdhury@utdallas.edu

Jing Qin
jing.qin@uky.edu

[1] Department of Mathematical Sciences, The University of Texas at Dallas, Richardson, TX 75080, USA

[2] Department of Mathematics, University of Kentucky, Lexington, KY 40506, USA

Published online: 25 August 2020

Author's personal copy

ods have been developed to regularize the solution based on various image priors. For example, Tikhonov-regularized deconvolution methods [31,66] rely on the least-squares estimation, which leads to over-smoothed image recovery results. Owing to an edge-preserving property, total variation (TV) [58] has become one of the most popular regularization techniques in image deconvolution [4,7,14,15,69]. However, the TV regularization often reduces the image contrast and produces staircasing artifacts. To compensate for these drawbacks, some variants of TV have been considered primarily for the Gaussian noise, such as the non-local TV [49], the total generalized variation (TGV) [47,56], and fractional-order TV (FOTV) [55]. It is worth noting that both FOTV and TGV achieve comparable performance [55], but FOTV is more efficient than TGV due to the infimal convolution of TGV that involves more unknown variables than FOTV. Therefore, we adopt the FOTV regularization in this work.

Blind image deblurring is significantly more challenging than the non-blind case, as it requires to estimate both the image and the kernel from a degraded image. One evident ambiguity is a relative scale between the sharp image and the blur. Jin et al. [33] showed a careful normalization of PSF yields significant improvements in blind deconvolution results in terms of accuracy and robustness to noise. Other types of ambiguities can be resolved by probabilistic approaches, e.g., simulated annealing [52], but with high computational costs. Krishnan et al. [35] proposed a normalized sparsity measure for blind deconvolution, while a plug-and-play approach was adopted in [48]. Motivated by the *PhaseLift* method [11] in phase retrieval, blind deconvolution was recast in [5] as reconstructing a rank-one matrix from a set of linear measurements. Recently, Li et al. [46] proposed to perform blind deconvolution and phase retrieval simultaneously via a low-rank recovery. Following the success of deep learning, some learning-based approaches for blind deconvolution include [1,38,45,61,65].

Since PSF plays a critical role in the blurring process, estimation of PSF can be either separated from or combined with non-blind approaches [12,17,37,70,72]. Along this line of research, the convolution kernel can be estimated by various variational methods, including expectation maximization (EM) and maximum a posterior (MAP) with local or global priors [23,43,63]. Please refer to [59] for variational Bayesian methods and [39] for a comprehensive comparison among various blind deblurring algorithms. In addition to smoothness assumptions of the underlying image, it is also plausible to impose certain smoothness for PSF, such as TV [16,73] and FOTV [75]. Unfortunately, the joint optimization of both kernel and image often leads to a no-blur solution [44], which can be avoided by sequentially projecting the kernel onto a feasible set of nonnegative and sum-to-one solutions [53].

In many applications, both blurring and Poisson noise occur in an obtained image. In contrast to Gaussian noise, Poisson noise is signal-dependent and non-additive, which brings additional challenges to image deconvolution. Image data subject to Poisson noise can be recovered by maximum likelihood and Bayesian approaches [8,67]. One of the most widely used deblurring methods to deal with Poisson noise is the Richardson–Lucy (RL) algorithm proposed independently by Richardson [57] and Lucy [50]. One common approach for deblurring under Poisson noise is based on the modification of the data fidelity from the least squares misfit (for Gaussian noise) to a logarithmic form (for Poisson noise). For example, TV-based Poisson deblurring methods include [20,24,42,62]. Similarly, frame-based method [30], non-local gradient [29], and a dictionary learning approach [51] were proposed to handle Poisson noise. Little attention has been paid on blind deblurring under Poisson noise, except for alternating minimization method [54], RL-based blind deblurring methods [9,25], and mixed Poisson–Gaussian noise [6].

1.2 Scope of the Paper

The goal of this work is to remove Poisson noise and blurring artifacts simultaneously from an observed image. Motivated by our recent FOTV Poisson denoising [18], we develop deblurring methods based on the FOTV regularization to preserve high-order smoothness of the underlying image. In particular, we consider both non-blind and blind deblurring models. We adopt the alternating direction method of multipliers (ADMM) [10,26,27] for the non-blind deconvolution and an EM-based optimization scheme [60,71] only for the blind case. A variety of numerical experiments on natural images have shown the great potential of the proposed algorithms in terms of visual quality and reconstruction accuracy. The major contributions of this work are threefold. First, we incorporate the FOTV regularization for image deblurring problem with Poisson noise. Second, we develop two efficient algorithms for solving non-blind and blind deconvolution models, respectively. Convergence guarantee is established for the blind case. Lastly, extensive experiments are conducted to demonstrate the superior performance of the proposed approaches, especially significant improvements over the state-of-the-art methods are observed in our blind deblurring algorithm.

The rest of the paper is organized as follows. Section 2 provides background knowledge on convolution models, Poisson noise statistics, the EM algorithm, and the definition of the FOTV regularization. The proposed models for both non-blind and blind deconvolution are described in Sect. 3 together with two efficient algorithms. Extensive experiments are presented in Sect. 4, illustrating the effectiveness and efficiency of our proposed methods. Finally, Sect. 5 concludes the paper.

Author's personal copy

2 Preliminaries

In this section, we briefly review a few key components of the proposed methods.

2.1 Convolution Models

The image blurring process can be modeled by a linear equation

$$g = h \circledast u, \tag{1}$$

where g is a blurred image by convolving a sharp image u with a blurring kernel h and $\circledast$ denotes a two-dimensional convolution operator. To properly define the convolution operator, we shall discuss boundary conditions of the image. There are several boundary conditions used in image deblurring, including *zero*, *periodic*, *reflexive* and *anti-reflexive* boundary conditions [21,28]. In particular, the periodic boundary condition has been commonly used in image processing, since the convolution operator under the periodic boundary condition can be efficiently implemented via the fast Fourier transform (FFT). However, since images are not always periodic, an alternative approach [53] is to restrict convolution to a smaller region rather than the original image so that the boundary conditions do not affect the acquired data, which is referred to as *no boundary condition*. A discrete image can be represented as a matrix. Let u be a matrix of size $m \times n$ and the kernel h of size $l \times w$. Following the Matlab's `valid` option in convolution, we denote

$$\bar{g} = h \circ u, \tag{2}$$

where $\bar{g}$ has the support of size $(m - l + 1) \times (n - w + 1)$. Note that h and u are not commutative, i.e., $h \circ u \not\equiv u \circ h$ in general, and $u \circ h$ may not be well-defined if the support of h is relatively small.

In this work, we use the periodic boundary condition (1) for the non-blind deconvolution and no boundary condition (2) for the blind case. With an abuse of notation, we denote both types of convolution as a matrix-vector multiplication after vectorizing the image u, denoted by Hu with a matrix H, in order to have a unified formulation. We will specify which convolution operator is used when discussing the corresponding algorithms.

2.2 Poisson Noise

Due to the physical mechanism of the imaging process, Poisson distribution is more appropriate to describe the noise statistics than the commonly used Gaussian distribution. Poisson noise, also known as photon noise, can be described by the Poisson distribution. Recall that a random variable f is said to follow a Poisson distribution with a parameter $\gamma > 0$, if the probability mass function is given by

$$\mathrm{Pr}_\gamma(f) = \frac{\gamma^f}{f!} \mathrm{e}^{-\gamma}.$$

The parameter γ determines the expected value of f as well as its variance. Now we assume the measured data at each pixel f_i follows an i.i.d. Poisson distribution with the ground-truth value g_i being the parameter γ (the expectation) and hence we have

$$\Pr(f|g) = \prod_{i=1}^{N} \frac{g_i^{f_i}}{f_i!} \mathrm{e}^{-g_i}. \tag{3}$$

Here N is the total number of pixels, $f = \{f_i\}_{i=1}^N$ with each $f_i \geq 0$, and $g = \{g_i\}_{i=1}^N$. From the Bayes' Theorem, the posterior probability density of g for a given f is

$$\Pr(g|f) = \frac{\Pr(f|g)\Pr(g)}{\Pr(f)}. \tag{4}$$

Taking the negative log-likelihood of (4), we get

$$\begin{aligned} &-\log \Pr(g|f) \\ &= \sum_{i=1}^{N} -f_i \log g_i + g_i + \log(f_i!) - \log \Pr(g) + \log \Pr(f) \\ &= \sum_{i=1}^{N} (g_i - f_i \log g_i) - \log \Pr(g) + (\log(f_i!) + \log \Pr(f)). \end{aligned} \tag{5}$$

The last two terms involving f are known and therefore can be ignored when minimizing (5) with respect to g.

We assume that the observed image f is obtained by the convolution of the clean image u with the blurring kernel h, followed by the corruption with Poisson noise. We can estimate the image u via the maximum a posteriori probability (MAP), i.e., $u \in \mathrm{argmax}_{u \geq 0} \Pr(u|f)$. Since the blur can be expressed as $g = Hu$, the posterior probability $\Pr(u|f)$ and the prior probability Pr(g) are related to $\Pr(g|f)$ and Pr(u), respectively. By using the log-likelihood form of (5), the MAP estimation can be expressed as,

$$\min_{u \geq 0} \langle (Hu - f \log Hu), \mathbf{1}_\Omega \rangle + R(u), \tag{6}$$

where $\mathbf{1}_\Omega$ denotes the indicator function on a discrete grid of the image domain $\Omega \subset \mathbb{R}^2$ and $R(u)$ is related to $-\log \Pr(u)$, which is called an image prior.

2.3 Expectation-Maximization

We review an expectation-maximization (EM) algorithm [19, 64] to minimize (6), which will be integrated in our algorithm.

Author's personal copy

Suppose that there is no prior probability, i.e., regularization term $R(u)=0$ and hence we have

$$\min_{u\geq 0}\langle (Hu - f\log Hu), \mathbf{1}_\Omega\rangle. \tag{7}$$

It follows from the Karush–Kuhn–Tucker (KKT) conditions [34,36] that there exists an Lagrange multiplier vector $\lambda \geq 0$ such that

$$0 = H^*\mathbf{1}_\Omega - H^*\left(\frac{f}{Hu}\right) - \lambda, \tag{8}$$

$$0 = \lambda \odot u, \tag{9}$$

where H^* is the adjoint operator of H and $\odot$ is the componentwise multiplication. Note that since H is a real matrix, H^* is simply the transpose of H.

After multiplying (8) by u componentwise and substituting into (9), we can get an updating scheme for u^{k+1} by the fixed-point iteration method

$$u^{k+1} = \frac{u^k}{H^*\mathbf{1}_\Omega} \odot H^*\left(\frac{f}{Hu^k}\right), \tag{10}$$

where vector multiplication and division are all componentwise. For simplicity, we omit the use of $\odot$ and define the following operator

$$\mathrm{EM}(f, H, u) = \frac{u}{H^*\mathbf{1}_\Omega} H^*\left(\frac{f}{Hu}\right), \tag{11}$$

which depends on f, H, u, and returns the output in (10). We can show the objective function (7) decreases under the iteration (10); please refer to Lemma 1 in "Appendix."

2.4 Fractional-Order Total Variation

We consider a fractional-order total variation as an image prior. Given an image domain $\Omega \subset \mathbb{R}^2$, we discretize it as a rectangular grid $\{(x_i, y_j) : 1 \leq i \leq m, 1 \leq j \leq n\}$. Then an image can be represented as a matrix in the Euclidean space $\mathbb{R}^{m\times n}$, denoted as $u_{i,j} = u(x_i, y_j)$. For a specified order $\alpha > 0$ of derivatives where α could be a fractional number, the α-order total variation of $u : \Omega \to \mathbb{R}$ extends the traditional TV [58] by involving fractional-order derivatives. In particular, based on the Grünwald-Letnikov fractional-order derivatives [74], the discrete fractional-order gradient is defined as

$$\nabla^\alpha u = [D_1^\alpha u, D_2^\alpha u]^{\mathrm{T}}, \tag{12}$$

where the fractional-order derivatives $D_1^\alpha u, D_2^\alpha u \in \mathbb{R}^{m\times n}$ along the x-axis and the y-axis are approximated by the

$$\begin{aligned}(D_1^\alpha u)_{i,j} &= \sum_{k=0}^{K-1}(-1)^k C_k^\alpha u_{i-k,j},\\ (D_2^\alpha u)_{i,j} &= \sum_{k=0}^{K-1}(-1)^k C_k^\alpha u_{i,j-k}.\end{aligned} \tag{13}$$

Here K is the number of neighboring pixels that are used to approximate the fractional-order derivative at each pixel. The coefficients $\{C_k^\alpha\}_{k=0}^{K-1}$ are defined as $C_k^\alpha = \frac{\Gamma(\alpha+1)}{\Gamma(k+1)\Gamma(\alpha+1-k)}$ with the Gamma function $\Gamma(x)$. Then the discrete fractional-order TV of u is defined as

$$\|\nabla^\alpha u\|_1 := \sum_{i,j}\left(|(D_1^\alpha u)_{i,j}| + |(D_2^\alpha u)_{i,j}|\right). \tag{14}$$

According to the relation that $(\nabla^\alpha)^* = \overline{(-1)^\alpha}\mathrm{div}^\alpha$, the discrete fractional-order divergence $\mathrm{div}^\alpha \boldsymbol{p} \in \mathbb{R}^{m\times n}$ for $\boldsymbol{p} = (p^{(1)}, p^{(2)}) \in \mathbb{R}^{m\times n}\times\mathbb{R}^{m\times n}$ is given by [74]

$$(\mathrm{div}^\alpha \boldsymbol{p})_{i,j} = (-1)^\alpha \sum_{k=0}^{K-1}(-1)^k C_k^\alpha (p^{(1)}_{i+k,j} + p^{(2)}_{i,j+k}). \tag{15}$$

Note that the divergence (15) is the adjoint of the gradient (12).

3 The Proposed Methods

We propose two FOTV-regularized variational models for non-blind and blind deconvolution under Poisson noise. More specifically, we incorporate the FOTV regularization (14) as an image prior $R(u)$ into the MAP estimation (6). Technically speaking, both non-blind and blind deconvolution can have the same objective function to be minimized, while the blind deconvolution requires an additional estimate of the kernel. Furthermore, we decide to use different boundary conditions for blind and non-blind deconvolutions. Since blind deconvolution is much more delicate than the non-blind one, we do not want to use any unfaithful information from wrongly assumed boundary conditions and hence the model (2) with a no-boundary-condition is more appropriate for blind deconvolution. As for the non-blind case, we adopt the periodic boundary condition (1) for fast computation.

3.1 Non-blind Deconvolution

We propose the following FOTV-regularized model for non-blind deconvolution, when the data are corrupted by Poisson noise,

$$\min_{u\in\Omega}\|\nabla^\alpha u\|_1 + \beta\langle h\circledast u - f\log(h\circledast u), \mathbf{1}_\Omega\rangle, \tag{16}$$

Author's personal copy

where $\beta > 0$ is a weighting parameter to make a balance between the regularization term and the data fitting. We adopt the alternating direction method of multipliers (ADMM) [10, 26,27] to solve the proposed model (16). In particular, we introduce two auxiliary variables $\mathbf{z} \in \mathbb{R}^{m\times n\times 2}$, $g \in \mathbb{R}^{m\times n}$, and reformulate (16) in an equivalent form,

$$\begin{aligned} &\min_{u,\mathbf{z},g} \|\mathbf{z}\|_1 + \beta\langle g - f\log(g), \mathbf{1}_\Omega\rangle, \\ &\quad \text{s.t.} \quad \mathbf{z} = \nabla^\alpha u, \;\; g = h \circledast u. \end{aligned} \tag{17}$$

The corresponding augmented Lagrangian functional is given by

$$\begin{aligned} \mathcal{L}(u, \mathbf{z}, g; \boldsymbol{\lambda}_1, \lambda_2) &= \|\mathbf{z}\|_1 + \beta\langle g - f\log g, \mathbf{1}_\Omega\rangle \\ &+ \langle \boldsymbol{\lambda}_1, \mathbf{z} - \nabla^\alpha u\rangle + \frac{\mu_1}{2}\left\|\mathbf{z} - \nabla^\alpha u\right\|_F^2 \\ &+ \langle \lambda_2, g - h \circledast u\rangle + \frac{\mu_2}{2}\|g - h\circledast u\|_F^2, \end{aligned} \tag{18}$$

where $\boldsymbol{\lambda}_1 \in \mathbb{R}^{m\times n\times 2}$ and $\lambda_2 \in \mathbb{R}^{m\times n}$ are dual variables or Lagrangian multipliers, μ_1, μ_2 are two positive parameters, and $\|\cdot\|_F$ denotes the Frobenius norm. Then ADMM yields the following iterations,

$$\begin{cases} u^{k+1} = \underset{u}{\operatorname{argmin}}\, \mathcal{L}(u, \mathbf{z}^k, g^k; \boldsymbol{\lambda}_1^k, \lambda_2^k), \\ \mathbf{z}^{k+1} = \underset{\mathbf{z}}{\operatorname{argmin}}\, \mathcal{L}(u^{k+1}, \mathbf{z}, g^k; \boldsymbol{\lambda}_1^k, \lambda_2^k), \\ g^{k+1} = \underset{g}{\operatorname{argmin}}\, \mathcal{L}(u^{k+1}, \mathbf{z}^{k+1}, g; \boldsymbol{\lambda}_1^k, \lambda_2^k), \\ \boldsymbol{\lambda}_1^{k+1} = \boldsymbol{\lambda}_1^k + \mu_1(\mathbf{z}^{k+1} - \nabla^\alpha u^{k+1}), \\ {\lambda_2}^{k+1} = {\lambda_2}^k + \mu_2(g^{k+1} - h\circledast u^{k+1}). \end{cases} \tag{19}$$

To solve the u-subproblem in (19), we compute the gradient of (18) with respect to u and get the optimality condition

$$(\nabla^\alpha)^*(\mu_1\nabla^\alpha u - \mu_1\mathbf{z} - \boldsymbol{\lambda}_1) + \tilde{h}\circledast(\mu_2 h\circledast u - \mu_2 g - \lambda_2) = 0.$$

Here $(\nabla^\alpha)^*$ is the adjoint of ∇^α, which is the divergence operator defined in (15), and $\tilde{h}$ is the adjoint kernel of h by rotating h by 90° clockwise. Under the periodic boundary condition, the composite operators $(\nabla^\alpha)^*(\nabla^\alpha\cdot)$ and $\tilde{h}\circledast(h\circledast\cdot)$ can be diagonalized by the fast Fourier transform (FFT) due to their respective circulant transformation matrices. Therefore, we obtain a closed-form solution for u given by

$$u^{k+1} = \mathcal{F}^{-1}\left(\frac{\mathcal{F}(v)}{\mu_1\mathcal{F}[(\nabla^\alpha)^*(\nabla^\alpha)] + \mu_2|\mathcal{F}(h)|^2}\right), \tag{20}$$

where $v = (\nabla^\alpha)^*(\mu_1\mathbf{z}^k + \boldsymbol{\lambda}_1^k) + \tilde{h}\circledast(\mu_2 g^k + \lambda_2^k)$, $\mathcal{F}$ and $\mathcal{F}^{-1}$ represent the Fourier transform and its inverse, respectively. Note that matrix division, square and absolute value are all performed componentwise.

Algorithm 1: FOTV non-blind deconvolution under Poisson noise.

```
Input: $f, h$
Set parameters: $\alpha, \beta, \mu_1, \mu_2, \epsilon > 0$
Initialization: $u^0 = f, g^0 = h \circledast u^0, \boldsymbol{\lambda}_1^0 = \mathbf{0}, \lambda_2^0 = 0, k = 0$
while $\frac{\|u^{k+1}-u^k\|_F}{\|u^k\|_F} < \epsilon$ do
    Solve $u^{k+1}$ by (20),
    Solve $\mathbf{z}^{k+1}$ by (21),
    Solve $g^{k+1}$ by (22),
    $\boldsymbol{\lambda_1}^{k+1} = \boldsymbol{\lambda_1}^k + \mu_1(\mathbf{z}^{k+1} - \nabla^\alpha u^{k+1})$,
    ${\lambda_2}^{k+1} = {\lambda_2}^k + \mu_2(g^{k+1} - h \circledast u^{k+1})$,
    $k \leftarrow k + 1$
end
Output: $u = u^{k+1}$.
```

In addition, there is a closed-form solution for the $\mathbf{z}$-subproblem given by a *shrinkage* operator,

$$\mathbf{z}^{k+1} = \operatorname{shrink}\left(\nabla^\alpha u^{k+1} - \frac{\boldsymbol{\lambda_1}^k}{\mu_1}, \frac{1}{\mu_1}\right), \tag{21}$$

where $\operatorname{shrink}(\mathbf{s}, \gamma) = \operatorname{sgn}(\mathbf{s})\odot\max\{|\mathbf{s}| - \gamma, 0\}$ with all arithmetic operators being performed componentwise.

Taking the derivative of the functional $\mathcal{L}$ with respect to g, we obtain the optimality condition for the g-subproblem,

$$\beta\left(1 - \frac{f}{g}\right) + \lambda_2 + \mu_2(g - h\circledast u^{k+1}) = 0.$$

Since $g > 0$, we rewrite the above equation as a quadratic equation

$$g^2 + \left(\frac{\beta + \lambda_2}{\mu_2} - h\circledast u^{k+1}\right)g - \frac{\beta f}{\mu_2} = 0,$$

and choose the positive solution, i.e.,

$$\begin{aligned} g^{k+1} = &\frac{-\left(\frac{\beta+\lambda_2^k}{\mu_2} - h\circledast u^{k+1}\right)}{2} \\ &+ \frac{\sqrt{\left(\frac{\beta+\lambda_2^k}{\mu_2} - h\circledast u^{k+1}\right)^2 + 4\left(\frac{\beta f}{\mu_2}\right)}}{2}. \end{aligned} \tag{22}$$

In summary, we present in Algorithm 1 for minimizing the FOTV regularized non-blind deconvolution problem (16) via ADMM.

3.2 Blind Deconvolution

Boundary conditions play an important role in the success of blind deconvolution methods. In fact, all the standard boundary conditions, i.e., periodic, reflexive, and zero, do not correspond to any imaging systems in practice and cause

Author's personal copy

unnatural artifacts such as ringing artifacts near boundaries [2,13]. To mitigate these artifacts along the boundaries, we assume to know the kernel size and crop the measured data f in such a way that the boundary condition has no effect on the objective function. For this purpose, we only consider the cropped convolution output without zero-padding of boundaries, which is implemented by choosing the `valid` option in Matlab's convolution. Suppose the original image u and the blurring kernel h are of sizes $m \times n$ and $l \times w$, respectively. The resulting no-boundary convolution of u and h, denoted by $u \circ h$, is of size $(m-l+1) \times (n-w+1)$. We further incorporate the nonnegativity and sum-to-one assumptions of the blurring kernel and obtain the following minimization problem for blind deconvolution

$$\min_{\substack{u\in\Omega\\ h\in\Pi}} \|\nabla^\alpha u\|_1 + \beta\langle h\circ u - \bar{f}\log(h\circ u), \mathbf{1}_\Omega\rangle, \tag{23}$$

where $\Pi = \{h \in \mathbb{R}^{l\times w} \,|\, h_{i,j} \geq 0, \sum_{i,j} h_{i,j} = 1\}$ and $\bar{f}$ is the cropped blurry observation. In what follows, we propose an alternating minimization algorithm to solve (23) for u and h.

We first minimize (23) with respect to u using a two-step EM approach [71]. Suppose we have u^k and h^k at the kth iteration. We define the convolution operation as a matrix-vector form, i.e.,

$$h^k \circ u = Hu.$$

Then the optimality condition of (23) with respect to u can be expressed as

$$\frac{1}{\beta} p^{k+1} + H^*\mathbf{1}_\Omega - H^*\Big(\frac{\bar{f}}{Hu^k}\Big) = 0, \tag{24}$$

where p^{k+1} is a subgradient of the functional $\|\nabla^\alpha \cdot\|_1$ at u^{k+1}, i.e., $p^{k+1} \in \partial\|\nabla^\alpha u^{k+1}\|_1$. Dividing (24) by $H^*\mathbf{1}_\Omega$ yields

$$\frac{1}{\beta H^*\mathbf{1}_\Omega} p^{k+1} + \mathbf{1}_\Omega - \frac{1}{H^*\mathbf{1}_\Omega} H^*\Big(\frac{\bar{f}}{Hu^k}\Big) = 0. \tag{25}$$

We insert $\frac{u^k}{u^{k+1}}$ into the last term as an approximation to the constant $\mathbf{1}_\Omega$, thus leading to an equation for u^{k+1},

$$\frac{1}{\beta H^*\mathbf{1}_\Omega} p^{k+1} + \mathbf{1}_\Omega - \frac{1}{H^*\mathbf{1}_\Omega} H^*\Big(\frac{\bar{f}}{Hu^k}\Big)\frac{u^k}{u^{k+1}} = 0. \tag{26}$$

Following the notation in (11), we define

$$u^{k+\frac{1}{2}} := \mathrm{EM}(\bar{f}, H, u^k), \tag{27}$$

which is referred to as the EM step. Then (26) can be rewritten as

$$\frac{1}{\beta H^*\mathbf{1}_\Omega} p^{k+1} + \mathbf{1}_\Omega - \frac{u^{k+\frac{1}{2}}}{u^{k+1}} = 0,$$

which implies that u^{k+1} is the optimal solution to

$$\min_{u\in\Omega} \|\nabla^\alpha u\|_1 + \beta\langle H^*\mathbf{1}_\Omega, u - u^{k+\frac{1}{2}}\log u\rangle. \tag{28}$$

We then minimize (28) via ADMM. In particular, we reformulate (28) as

$$\begin{aligned} &\min_{u\in\Omega} \|\mathbf{v}\|_1 + \beta\langle H^*\mathbf{1}_\Omega, u - u^{k+\frac{1}{2}}\log u\rangle \\ &\text{s.t.} \quad \mathbf{v} = \nabla^\alpha z, \quad z = u, \end{aligned} \tag{29}$$

with two auxiliary variables v and z. The corresponding augmented Lagrangian functional reads as

$$\begin{aligned} \mathcal{L}(u, \mathbf{v}, z; \boldsymbol{\lambda_1}, \lambda_2) = {} & \|\mathbf{v}\|_1 + \beta\langle H^*\mathbf{1}_\Omega, u - u^{k+\frac{1}{2}}\log u\rangle \\ & + \frac{\mu_1}{2}\|\mathbf{v} - \nabla^\alpha z + \frac{\boldsymbol{\lambda}_1}{\mu_1}\|_F^2 + \frac{\mu_2}{2}\|z - u + \frac{\lambda_2}{\mu_2}\|_F^2. \end{aligned} \tag{30}$$

Here $\boldsymbol{\lambda_1}, \lambda_2$ are dual variables and μ_1, μ_2 are positive penalty parameters. The ADMM iterations go as follows,

$$\begin{cases} u^{k+1} = \operatorname*{argmin}_u \mathcal{L}(u, \mathbf{v}^k, z^k; \boldsymbol{\lambda}_1^k, \lambda_2^k), \\ \mathbf{v}^{k+1} = \operatorname*{argmin}_{\mathbf{v}} \mathcal{L}(u^{k+1}, \mathbf{v}, z^k; \boldsymbol{\lambda}_1^k, \lambda_2^k), \\ z^{k+1} = \operatorname*{argmin}_z \mathcal{L}(u^{k+1}, \mathbf{v}^{k+1}, z; \boldsymbol{\lambda}_1^k, \lambda_2^k), \\ \boldsymbol{\lambda_1}^{k+1} = \boldsymbol{\lambda_1}^k + \mu_1(\mathbf{v}^{k+1} - \nabla^\alpha u^{k+1}), \\ \lambda_2^{k+1} = \lambda_2^k + \mu_2(z^{k+1} - u^{k+1}). \end{cases} \tag{31}$$

Similarly to the non-blind case, we derive the closed-form solution for the u-subproblem by using the positive solution of the quadratic equation

$$\beta C(1 - \frac{u^{k+\frac{1}{2}}}{u}) - \lambda_2 - \mu_2(z - u) = 0,$$

for $C = H^*\mathbf{1}_\Omega$. Therefore, we get

$$\begin{aligned} u^{k+1} = {} & \frac{-(\beta C - \mu_2 z^k - \lambda_2)}{2\mu_2} \\ & + \frac{\sqrt{(\beta C - \mu_2 z^k - \lambda_2)^2 + 4\mu_2\beta C u^{k+\frac{1}{2}}}}{2\mu_2}, \end{aligned} \tag{32}$$

Author's personal copy

The $\mathbf{v}$-subproblem can be minimized via the shrinkage operator,

$$\mathbf{v}^{k+1} = \operatorname{shrink}\left(\nabla^\alpha z^k - \frac{\boldsymbol{\lambda_1}^k}{\mu_1}, \frac{1}{\mu_1}\right), \tag{33}$$

and we have the following z-update,

$$z^{k+1} = \mathcal{F}^{-1}\left(\frac{\mathcal{F}(\mu_2 u^{k+1} + \mu_1(\nabla^\alpha)^*\mathbf{v}^{k+1} + (\nabla^\alpha)^*\boldsymbol{\lambda_1} - \lambda_2)}{\mathcal{F}(\mu_1(\nabla^\alpha)^*\nabla^\alpha + \mu_2)}\right). \tag{34}$$

To minimize (23) with respect to h, we define a matrix U in such a way that the convolution can be written as a matrix-vector multiplication,

$$h \circ u^{k+1} = Uh.$$

Since u and h are symmetric in the data fitting term, we can apply an EM step for h, i.e.,

$$h^{k+\frac{1}{2}} := \operatorname{EM}(\bar{f}, U, h^k).$$

Since h has the sum-to-one restriction, we then project $h^{k+\frac{1}{2}}$ to the corresponding affine space,

$$h^{k+1} = h^{k+\frac{1}{2}} / \sum_{ij} h_{ij}^{k+\frac{1}{2}}.$$

Note that the nonnegativity holds automatically from the EM step (11). We summarize the proposed algorithm for blind deconvolution under Poisson noise in Algorithm 2. Convergence of the proposed algorithm is characterized in Theorem 1.

Theorem 1 *For the sequence $\{u^k, h^k\}_{k=1}^\infty$ generated by Algorithm 2, there always exists a convergent subsequence of $\{u^k, h^k\}_{k=1}^\infty$.*

Please refer to "Appendix" for the detailed proof.

4 Numerical Experiments

In this section, we conduct a variety of numerical experiments to justify the effectiveness of the proposed methods in removing Poisson noise and blurring artifacts. We consider two types of blurring kernels for Gaussian blur and motion blur as well as several peak levels for different amount of Poisson noise.

Algorithm 2: FOTV blind deconvolution under Poisson noise.

```
Input: $\bar{f}$ and $l$ (kernel size)
Set parameters: $\alpha, \mu_1, \mu_2, \beta, \epsilon > 0$
Initialization: $\mathbf{v}^0 = \mathbf{0}, z^0 = 0, u^0 = \bar{f}$, $h^0$ to be an average kernel of size $l \times l$, $k = 0$
while $\frac{\|u^{k+1} - u^k\|_F}{\|u^k\|_F} < \epsilon$ do
    $u^{k+\frac{1}{2}} = \frac{u^k}{H^*\mathbf{1}_\Omega} H^*\left(\frac{\bar{f}}{Hu^k}\right)$
    $u^{k+1} = \frac{-p + \sqrt{p^2 + 4\mu_2\beta C u^{k+\frac{1}{2}}}}{2\mu_2}$
    where $p = (\beta C - \mu_2 z^k - \lambda_2)$
    $\mathbf{v}^{k+1} = \operatorname{shrink}(\nabla^\alpha z^k - \frac{\boldsymbol{\lambda_1}^k}{\mu_1}, \frac{1}{\mu_1})$,
    $z^{k+1}$ is given by (34)
    $\boldsymbol{\lambda_1}^{k+1} = \boldsymbol{\lambda_1}^k + \mu_1(\mathbf{v}^{k+1} - \nabla^\alpha u^{k+1})$,
    $\lambda_2^{k+1} = \lambda_2^k + \mu_2(z^{k+1} - u^{k+1})$,
    $h^{k+\frac{1}{2}} = \frac{h^k}{U^*\mathbf{1}_\Omega} U^*(\frac{\bar{f}}{Uh^k})$
    $h^{k+1} = h^{k+\frac{1}{2}} / \sum_{ij} h_{ij}^{k+\frac{1}{2}}$
    $k \leftarrow k + 1$
end
Output: $u = u^{k+1}, h = h^{k+1}$.
```

We use the peak signal-to-noise ratio (PSNR) and structural similarity (SSIM) index [68] for quantitative comparison. The PSNR is defined as

$$\operatorname{PSNR}(u, \bar{u}) = 10 \log_{10} \frac{P^2}{\frac{1}{mn}\sum_{i,j}(u_{i,j} - \bar{u}_{i,j})^2}, \tag{35}$$

where P is the maximum peak value of the original image $\bar{u} \in \mathbb{R}^{m \times n}$, and u is the restored image. As for SSIM, we define the *local* similarity index computed on two small patches x and y,

$$\operatorname{ssim}(x, y) = \frac{(2\mu_x\mu_y + c_1)(2\sigma_{xy} + c_2)}{(\mu_x^2 + \mu_y^2 + c_1)(\sigma_x^2 + \sigma_y^2 + c_2)}, \tag{36}$$

where μ_x/σ_x^2, μ_y/σ_y^2 are the average/variance of x, y, σ_{xy} is the covariance of x, y, and two positive parameters c_1, c_2 are set to avoid the denominator being zero. The overall SSIM is the mean of local similarity indexes, i.e.,

$$\operatorname{SSIM}(u, \bar{u}) = \frac{1}{K}\sum_{i=1}^{K} \operatorname{ssim}(x_i, y_i), \tag{37}$$

where x_i, y_i are the corresponding patches indexed by i in the two images $u, \bar{u}$, respectively, and K is the number of patches.

All numerical experiments are performed under Windows 7 and Matlab R2019b running on a desktop with Intel(R)

Author's personal copy

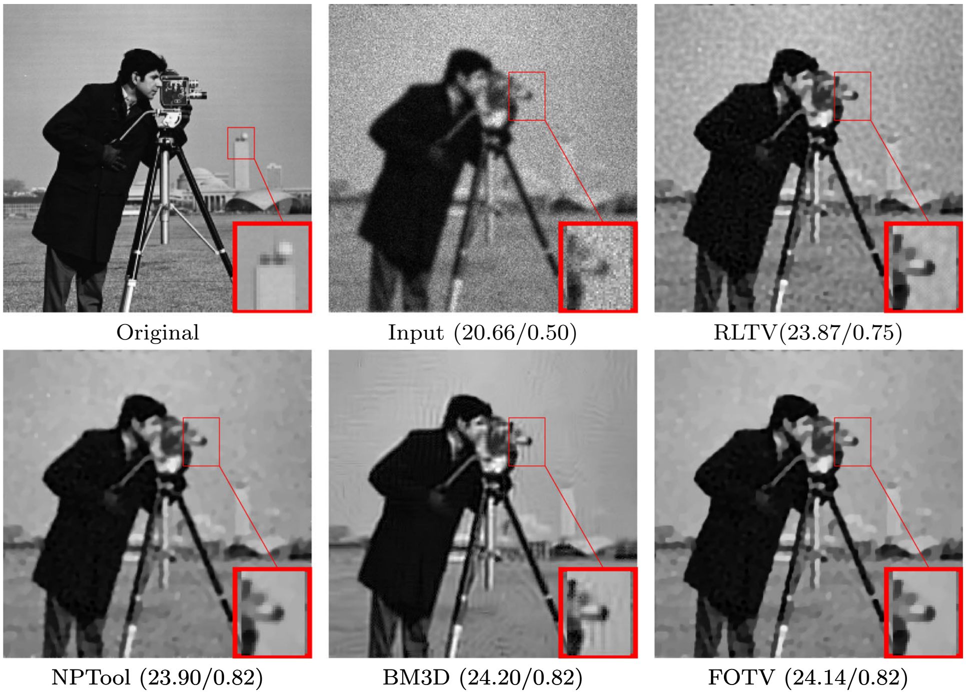
Original | Input (20.66/0.50) | RLTV(23.87/0.75)
NPTool (23.90/0.82) | BM3D (24.20/0.82) | FOTV (24.14/0.82)

Fig. 1 Non-blind deconvolution results of Cameraman with peak at $P/2 = 127.5$

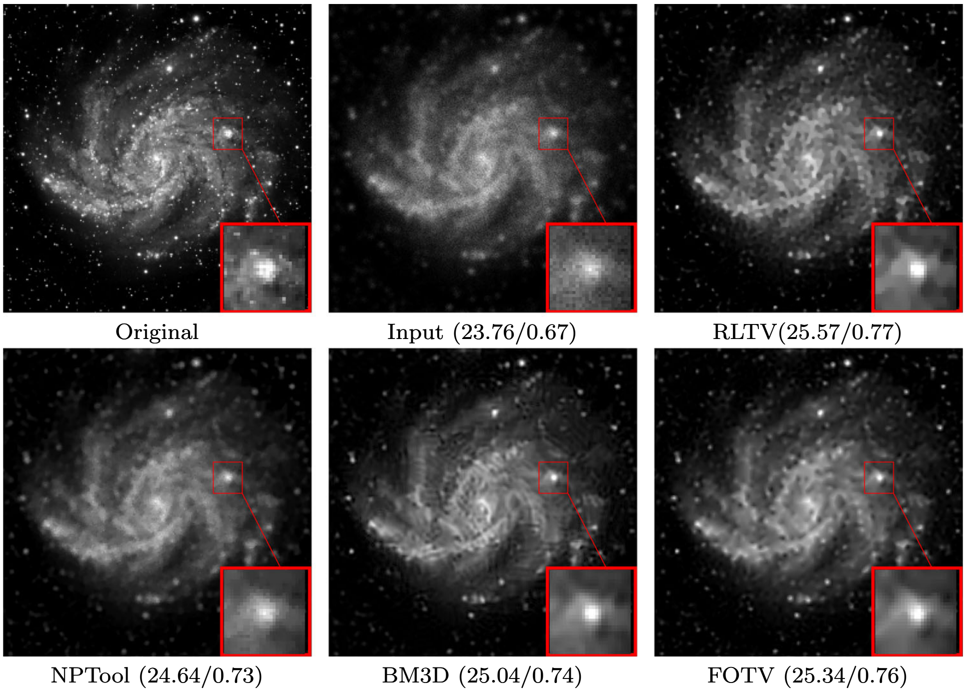
Original | Input (23.76/0.67) | RLTV(25.57/0.77)
NPTool (24.64/0.73) | BM3D (25.04/0.74) | FOTV (25.34/0.76)

Fig. 2 Non-blind deconvolution results of Galaxy with peak at $P = 255$.

Core(TM) i7-4790 CPU @3.60 GHz. Our Matlab source codes are available at GitHub.[1]

4.1 Non-blind Deconvolution

For the non-blind deconvolution experiments, we use the four standard testing images, named by "Cameraman," "Galaxy," "Phantom," and "Shape" as shown in Figs. 1, 2, 3 and 4, respectively. We consider the blurring kernel to be a 9×9 Gaussian kernel with standard deviation $\sqrt{3}$, i.e., `fspecial('gaussian',9,sqrt(3))` in Matlab.

---

[1] Our codes are at https://github.com/mujib2020/Non-blind-and-Blind-Deconvolution-under-Poisson-noise.

Author's personal copy

Fig. 3 Non-blind deconvolution results of Phantom with peak at $P/5 = 51$

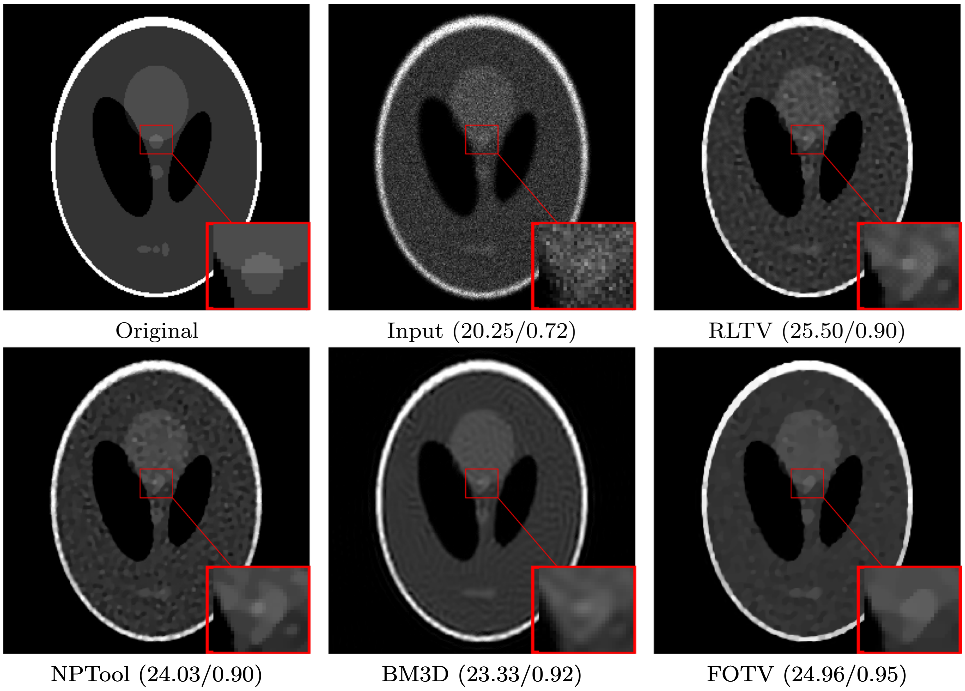

Original

Input (20.25/0.72)

RLTV (25.50/0.90)

NPTool (24.03/0.90)

BM3D (23.33/0.92)

FOTV (24.96/0.95)

Fig. 4 Non-blind deconvolution results of shape with peak at $P/10 = 25.5$

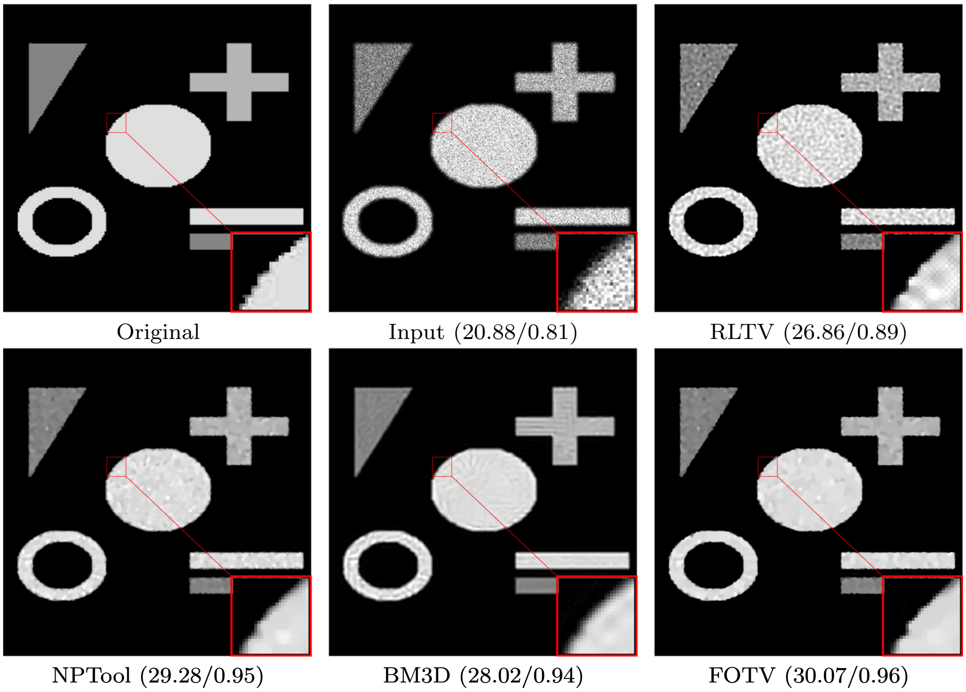

Original

Input (20.88/0.81)

RLTV (26.86/0.89)

NPTool (29.28/0.95)

BM3D (28.02/0.94)

FOTV (30.07/0.96)

Before taking a convolution, we set the peak value, i.e., the maximum intensity, to P, $P/2$, $P/5$, $P/10$ with $P = 255$, each corresponding to a level of Poisson noise. The smaller the peak is, the more noisy the image looks like, and hence, it becomes more challenging for deblurring/denoising.

We compare the proposed non-blind approach (Algorithm 1) with some Poisson deblurring methods, including TV regularized Richardson–Lucy (RLTL).[2] [22], NPTool [40], and BM3D [3]. For each image and each peak level, we choose the optimal parameters that achieve the highest PSNR among the sets: $\alpha \in \{1, 1.2, 1.6, 1.8\}$, $\beta \in \{10, 20, 50, 100, 150\}$, $\mu_1 \in \{0.01, 0.1, 1\}$, and $\mu_2 \in \{0.1, 1, 10, 20\}$. Note that we choose a large set of values for

---

[2] We download the Matlab package for RLTV from http://fxdupe.free.fr/software.html.

Author's personal copy

Table 1 Non-blind deconvolution comparison

Test image	Peak ($P = 255$)	Input	RLTV	NPTool	BM3D	FOTV
Cameraman	P	21.68/0.59	24.49/0.79	23.74/0.82	24.56/0.84	**24.59/0.84**
	$P/2$	20.66/0.50	23.87/0.75	23.90/0.82	**24.20/0.82**	24.14/**0.82**
	$P/5$	18.52/0.37	22.55/0.63	23.21/0.80	**23.58/0.80**	23.40/**0.80**
	$P/10$	16.30/0.29	20.96/0.51	22.49/0.77	**23.09/0.78**	22.75/0.75
Galaxy	P	23.76/0.67	**25.57/0.77**	24.64/0.73	25.04/0.74	25.34/0.76
	$P/2$	23.18/0.63	**24.99/0.74**	24.28/0.70	24.66/0.72	24.90/0.73
	$P/5$	21.83/0.55	24.24/0.70	24.12/0.70	24.14/0.69	**24.38/0.71**
	$P/10$	20.29/0.48	23.28/0.64	23.83/0.68	23.77/0.67	**23.86/0.67**
Phantom	P	21.27/0.85	27.49/0.96	24.39/0.89	24.61/0.93	**27.80/0.96**
	$P/2$	21.01/0.80	**27.11**/0.95	24.11/0.86	24.01/0.93	26.76/**0.96**
	$P/5$	20.25/0.72	**25.50**/0.90	24.03/0.90	23.33/0.92	24.96/**0.95**
	$P/10$	19.33/0.67	23.99/0.85	22.88/0.88	22.87/0.93	**24.17/0.93**
Shape	P	25.52/0.88	32.94/0.97	33.34/0.98	30.14/0.97	**34.32/0.99**
	$P/2$	24.61/0.85	31.50/0.95	29.97/0.94	29.53/0.94	**33.50/0.99**
	$P/5$	22.80/0.83	28.86/0.91	30.90/0.96	28.63/0.95	**31.77/0.98**
	$P/10$	20.88/0.81	26.86/0.89	29.28/0.95	28.02/0.94	**30.07/0.96**

Each entry contains PSNR and SSIM values. The best results are highlighted in bold

β to accommodate all the testing cases (different images/peak values). NPTool requires only one parameter, which is chosen among $\{10^{-5}, 2 \times 10^{-5}, 7 \times 10^{-5}, 10^{-4}, 2 \times 10^{-4}, 3 \times 10^{-4}, 9 \times 10^{-4}\}$. No parameter is needed for the other methods (RLTV and BM3D). The initial condition for all these methods is set to the input image. For our method, the stopping condition is $\frac{\|u^{k+1}-u^k\|_F}{\|u^k\|_F} < 10^{-4}$.

Quantitative comparisons in terms of PSNR and SSIM are reported in Table 1. The proposed algorithm achieves the best performance in most cases. For Cameraman under low peak values, BM3D is the winner, as it exploits similar patches to enhance the image denoising. For other three images, the image contents are relatively simple, i.e., having piecewise smooth structures, where FOTV performs particularly well. Visual comparisons are given in Figs. 1, 2, 3 and 4. We observe the proposed algorithm generally produces sharper results compared to other methods. Specifically for low peak values (51 and 25.5) in Figs. 3 and 4, the FOTV regularization can preserve piecewise smooth structures well and produce satisfactory deblurring (denoising) results. In the cases when BM3D and RLTV give higher PSNR values than FOTV, the recovered images are not visually pleasant with certain artifacts. For example, BM3D contains ringing artifacts, especially around the camera (see zoomed-in regions in Fig. 1). RLTV tends to amplify the noise, as shown in Fig. 3.

4.2 Non-blind Versus Blind

Before presenting the results of blind deconvolution, we compare two proposed algorithms for non-blind and blind deconvolution using the same input data of a blurry noisy Shape image with the same Gaussian kernel as used in the non-blind case (Sect. 4.1) with a peak value of 255. In Fig. 5, we plot the objective (energy) function and PSNR values with respect to time, which empirically shows the convergence of the proposed algorithms.

We present the deblurring results of shape and satellite in Figs. 6 and 7, respectively. Both are blurred with the same Gaussian kernel as used in the non-blind case with a peak value of 255. For a simple ground-truth image (Shape), both non-blind and blind deblurring algorithms yield satisfactory results, and the non-blind result is slightly better than the blind one. For a complicated image with more features (Satellite), the results are worse than Shape in terms of PSNR. This suggests that as a much more ill-posed problem, blind deconvolution cannot handle as much noise as in the non-blind case and hence we increase the peak value to `1e+03` so that the input data is less noisy.

For a fair comparison, we include comparisons using an EM-based blind deconvolution algorithm, which alternately updates the image and the kernel via (11) and adopt the same framework of EM-FOTV (Algorithm 2) to implement the EM algorithm, as summarized in Algorithm 3. In addition, we also consider the Tikhonov regularized blind deconvolution model given by,

$$\min_{\substack{u\in\Omega\\ h\in\Pi}} \beta\langle h \circ u - \bar{f}\log(h \circ u), \mathbf{1}_\Omega\rangle + \frac{1}{2}\|u\|_F^2, \tag{38}$$

where Π and $\mathbf{1}_\Omega$ are the same as in (23). We adopt the same update for h^k as in Algorithm 2. As for the u-subproblem,

Author's personal copy

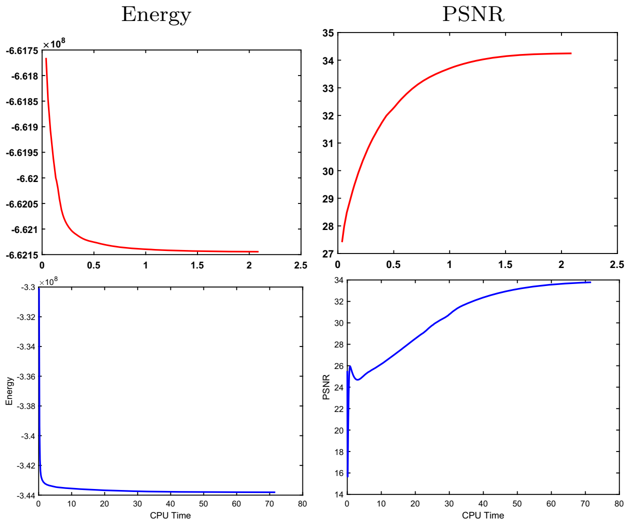

Fig. 5 Energy and PSNR curves (Shape image with peak at $P = 255$) for the non-blind (top) and blind (bottom) algorithms

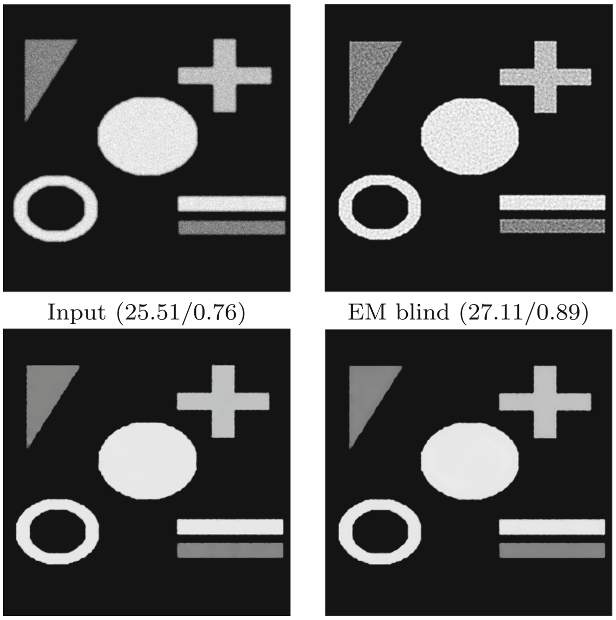
Input (25.51/0.76) EM blind (27.11/0.89)

FOTV non-blind (34.32/0.99) FOTV blind (33.78/0.99)

Fig. 6 Blind and non-blind comparison with the same input data: the Shape image blurred with the Gaussian kernel and peak value of 255

we consider

$$\min_{u \in \Omega} \beta \langle Hu - \bar{f} \log(Hu), \mathbf{1}_\Omega \rangle + \frac{1}{2}\|u\|_F^2, \tag{39}$$

where $Hu = h^k \circ u$. The optimality condition of (39) can be expressed as

$$\beta H^* 1_\Omega - \beta H^* \frac{\bar{f}}{Hu} + u = 0. \tag{40}$$

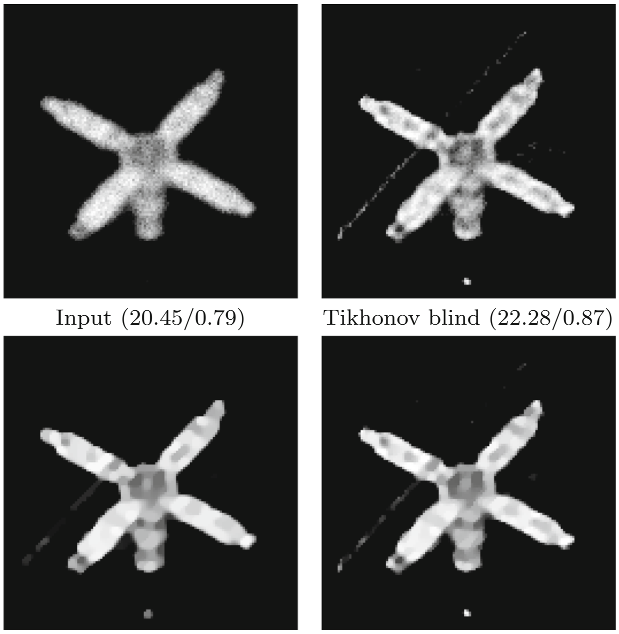
Input (20.45/0.79) Tikhonov blind (22.28/0.87)

FOTV non-blind (22.74/0.87) FOTV blind (22.52/0.87)

Fig. 7 Blind and non-blind comparison with the same input data: the satellite image blurred with the Gaussian kernel and peak value of 255

Algorithm 3: Blind deconvolution via EM.

```
Input: $\bar{f}$ and $l$ (the size of the kernel)
Set Parameter: $\epsilon > 0$
Initialization: $u^0 = f$, $h^0$ as an average kernel of size $l \times l$, $k = 0$
while $\frac{\|u^{k+1} - u^k\|_F}{\|u^k\|_F} < \epsilon$ do
    $u^{k+\frac{1}{2}} = \frac{u^k}{H^* \mathbf{1}_\Omega} H^* \left( \frac{\bar{f}}{Hu^k} \right)$
    $h^{k+\frac{1}{2}} = \frac{h^k}{U^* \mathbf{1}_\Omega} U^* ( \frac{\bar{f}}{Uh^k} )$
    $h^{k+1} = h^{k+\frac{1}{2}} / \sum h^{k+\frac{1}{2}}$
    $k \leftarrow k + 1$
end
Output: $u = u^{k+1}$, $h = h^{k+1}$.
```

Dividing (40) by $\beta H^* \mathbf{1}_\Omega$ and inserting $\frac{u^k}{u^{k+1}}$ into the second term to approximate the constant $\mathbf{1}_\Omega$, we get an equation for u^{k+1}, i.e.,

$$\mathbf{1}_\Omega - \frac{1}{H^* \mathbf{1}_\Omega} H^* \left(\frac{\bar{f}}{Hu^k} \right) \frac{u^k}{u^{k+1}} + \frac{u^k}{\beta H^* \mathbf{1}_\Omega} = 0. \tag{41}$$

Following the notation in (11), we can rewrite (41) as,

$$\mathbf{1}_\Omega - \frac{u^{k+\frac{1}{2}}}{u^{k+1}} + \frac{u}{\beta H^* \mathbf{1}_\Omega} = 0, \tag{42}$$

which implies that u^{k+1} is the optimal solution to

$$\min_u \ \beta \langle H^* \mathbf{1}_\Omega, u - u^{k+\frac{1}{2}} \log u \rangle + \frac{1}{2}\|u\|_F^2. \tag{43}$$

Author's personal copy

Table 2 Blind deconvolution comparison in terms of PSNR/SSIM

Test image	Kernel	Peak	Input	EM	Tikhonov	FOTV
Shape	Gaussian	255	25.51/0.87	22.31/0.86	28.97/0.92	33.78/0.99
	Motion	255	23.43/0.85	24.21/0.87	24.39/0.88	31.79/0.99
Spine	Gaussian	255	27.86/0.80	28.68/0.82	29.38/0.84	35.90/0.97
	Gaussian	`1e+03`	30.38/0.91	32.76/0.92	33.07/0.92	37.50/0.98
Satellite	Gaussian	`1e+03`	19.62/0.75	23.05/0.90	23.38/0.90	24.17/0.91
	Motion	`1e+03`	19.79/0.79	21.24/0.90	24.15/0.93	24.93/0.93

Setting the derivative of (43) with respect to u to zero, we get

$$\beta H^*\mathbf{1}_\Omega - \beta H^*\mathbf{1}_\Omega \frac{u^{k+\frac{1}{2}}}{u} + u = 0.$$

Therefore, u^{k+1} can be obtained by using the positive solution from the quadratic formula, i.e.,

$$u^{k+1} = \frac{-\beta H^*\mathbf{1}_\Omega}{2} + \frac{\sqrt{(\beta H^*\mathbf{1}_\Omega)^2 + 4\beta H^*\mathbf{1}_\Omega u^{k+\frac{1}{2}}}}{2}. \tag{44}$$

The Tikhonov-based regularization for blind deconvolution is summarized int Algorithm 4.

In Fig. 6, we use the ground-truth kernel as an initial guess for the EM algorithm, which is still worse than the proposed ones. Note that the EM approach is very sensitive to initial conditions and fails when the average kernel is set as the initial guess of the kernel. The comparison to Tikhonov is shown in Fig. 7.

Algorithm 4: Tikhonov blind deconvolution under Poisson noise.

```
Input: $\bar{f}$ and $l$ (the size of the kernel)
Set Parameter: $\beta, \epsilon > 0$
Initialization: $u^0 = f, h^0$ as an average kernel of size $l \times l$, $k = 0$
while $\frac{\|u^{k+1} - u^k\|_F}{\|u^k\|_F} < \epsilon$ do
    $u^{k+\frac{1}{2}} = \frac{u^k}{H^*\mathbf{1}_\Omega} H^* \left(\frac{\bar{f}}{Hu^k}\right)$
    $u^{k+1} = \frac{-\beta H^*\mathbf{1}_\Omega}{2} + \frac{\sqrt{(\beta H^*\mathbf{1}_\Omega)^2 + 8\beta H^*\mathbf{1}_\Omega u^{k+\frac{1}{2}}}}{2}$
    $h^{k+\frac{1}{2}} = \frac{h^k}{U^*\mathbf{1}_\Omega} U^*(\frac{\bar{f}}{Uh^k})$
    $h^{k+1} = h^{k+\frac{1}{2}} / \sum h^{k+\frac{1}{2}}$
    $k \leftarrow k + 1$
end
Output: $u = u^{k+1}, h = h^{k+1}$.
```

4.3 Blind Deconvolution

We conduct blind deconvolution using three testing images: Shape, Spine, and Satellite with two types of blurring kernels: Gaussian (`fspecial('gaussian',7,10)`) and motion blur (`fspecial('motion',11,45)`). For the

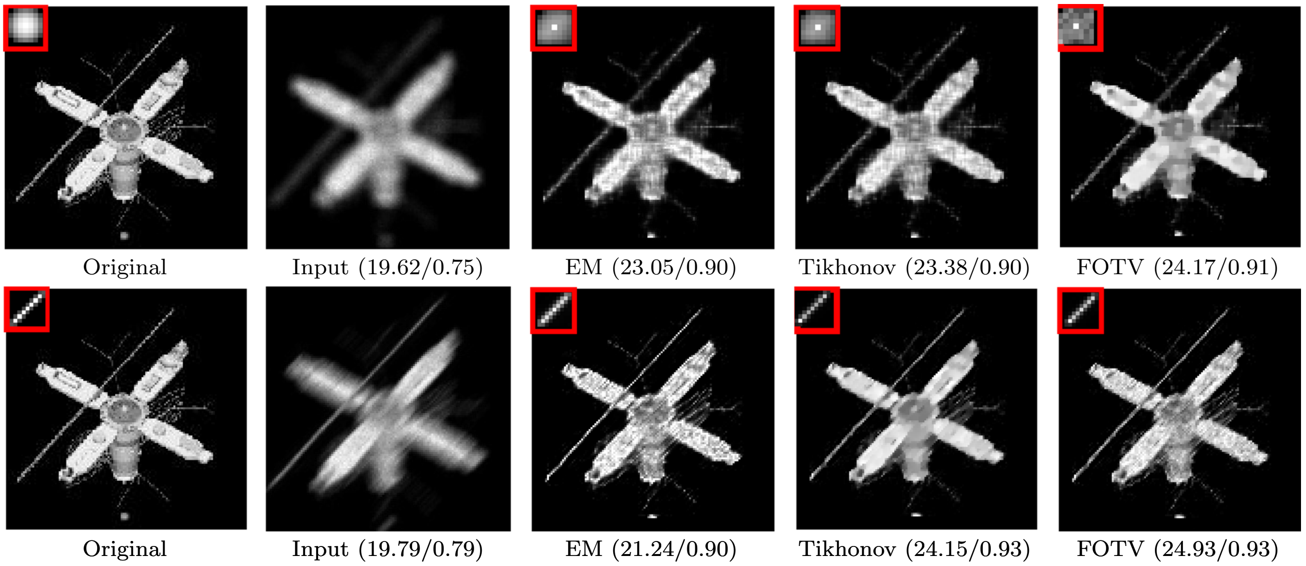

Original

Input (19.62/0.75)

EM (23.05/0.90)

Tikhonov (23.38/0.90)

FOTV (24.17/0.91)

Original

Input (19.79/0.79)

EM (21.24/0.90)

Tikhonov (24.15/0.93)

FOTV (24.93/0.93)

Fig. 8 Blind deconvolution results of Satellite image with peak at `1e+03`. The red box in the left corner shows the blurring kernel: Gaussian blur (top) and motion blur (bottom). The proposed algorithm works particularly well in estimating motion kernels (Color figure online)

Author's personal copy

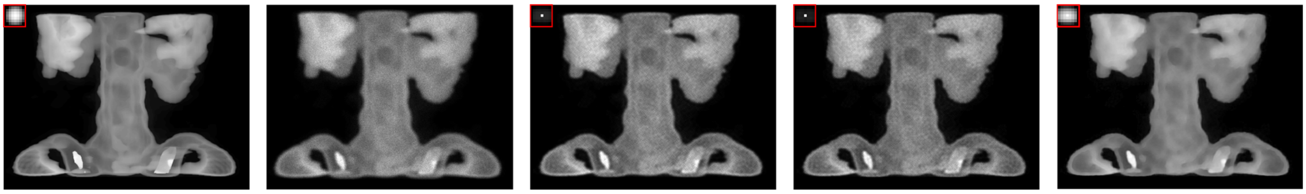

Original | Input (27.86/0.80) | EM (28.68/0.82) | Tikhonov (29.38/0.84) | FOTV (35.90/0.97)

Original | Input (30.38/0.91) | EM (32.76/0.92) | Tikhonov (33.07/0.92) | FOTV (37.50/0.98)

Fig. 9 Blind deconvolution results of the Spine image with Gaussian blur and peak values of 255 (top) and `1e+03` (bottom)

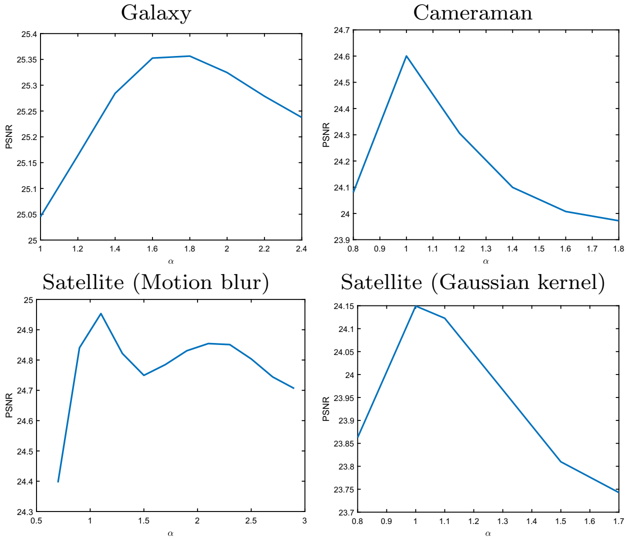

Fig. 10 PSNR versus fractional order α for Galaxy, Cameraman, Satellite all with peak values at 255. Top row is non-blind and bottom row is blind

Table 3 Optimal parameter settings

Peak	Cameraman					Galaxy				
	α	β	μ_1	μ_2	PSNR	α	β	μ_1	μ_2	PSNR
P	1	100	0.1	1	24.59	1.8	100	0.01	0.1	25.35
$P/2$	1	50	1	0.1	24.14	1.6	50	0.1	20	24.90
$P/5$	1	20	1	1	23.40	1.8	20	0.1	20	24.38
$P/10$	1	20	1	0.1	22.67	1.6	20	0.1	20	23.86

Shape image, we consider the same level of peak (255) but with two different types of blur. For the Spine image, we consider the same type of blur, but with two peak values (255 and `1e+03`). Since the Satellite image has finer features than the Shape image, we consider a higher peak value of `1e+03` with different types of blur.

We compare the proposed Algorithm 2 with EM (Algorithm 3) and Tikhonov (Algorithm 4). We select a set of optimal parameters of $\alpha \in \{1, 1.1\}, \beta \in \{10, 22, 60, 110, 200, 300\}$, $\mu_1 \in \{0.001, 0.01, 0.1\}$, and $\mu_2 \in \{0.01, 0.1, 0.5, 1\}$. The maximum iterations are chosen among 50, 100, 150, 250, 300, 1000 for the best performance. In addition, we choose the input data and the average kernel to be the initial guesses for u^0, h^0, respectively. The same initial guesses are chosen for EM and Tikhonov. The quantitative results are listed in Table 2, which implies significant improvements of the proposed algorithm over the classic ones. We also show visual results in Figs. 8 and 9 for Satellite and Spine, respectively. The proposed algorithm works particularly well for the motion blur. In addition, the EM results are consistent with the well-known phenomenon that blind deconvolution methods tend to obtain a no-blur solution [43,53], i.e., the estimated kernel looks like a delta function.

4.4 Discussion

We analyze the influence of the fractional-order α on the deblurring performance by plotting the PSNR curves versus α in Fig. 10. For each α, we tune the best combination of other parameters as discussed in Sect. 4.1. The optimal order for the Cameraman image is $\alpha = 1$, as the image is piecewise constant. Other images with more features have larger values of α, e.g., $\alpha = 1.8$ for the Galaxy image and $\alpha = 1.1$ for the Satellite image. We also list the optimal parameters in Table 3 for Cameraman and Galaxy, which shows that the optimal balancing parameter β consistently decreases with the peak values of images. The optimal values for μ_1, μ_2 are roughly the same for different peak values.

We report the computation time of various methods for both non-blind and blind deconvolution in Table 4. The proposed Algorithm 1 is much faster compared to the state-

Author's personal copy

Table 4 Computation time (in s)

Test image (size)	RLTV	NPTool	BM3D	FOTV (non-blind)	EM (blind)	Tikhonov (blind)	FOTV (blind)
Cameraman (256 × 256)	0.62	8.65	2.71	1.37	–	–	–
Shape (400 × 400)	2.74	14.69	12.62	4.63	0.40	28.97	37.63
Satellite (128 × 128)	–	–	–	–	0.16	1.75	2.05

The notation "–" indicates the nonexistence of the testing case, e.g., Cameraman is not used in blind deconvolution

of-the-art methods in non-blind deconvolution of Poisson noise. Our blind deconvolution algorithm is slower than the non-blind version, which is due to the nature of a gradient-descent type of algorithm, i.e., ensuring the stability but at the cost of slowing down the convergence.

5 Conclusions

In this paper, we consider the problem of recovering images that are contaminated by the Poisson noise with and without the prior information of the blurring kernel. To preserve the high-order smoothness, we propose the non-blind and blind image deconvolution models based on the fractional-order TV regularization and the statistical properties of Poisson noise. Efficient algorithms are derived by applying ADMM and EM with theoretical guarantees. Extensive experiments have shown that our proposed methods have the great potential in recovering sharper images from blurry ones subject to Poisson noise with high accuracy and efficiency. Future works include speed-up both non-blind and blind deconvolution algorithms with guaranteed convergence as well as proper regularization to be imposed on the blurring kernel.

Appendix

Based on the blind deconvolution model (23), we define the objective function

$$Q(u,h) := \|\nabla^\alpha u\|_1 + \beta\langle h\circ u - \bar{f}\log(h\circ u), \mathbf{1}_\Omega\rangle. \tag{45}$$

The proof of Theorem 1 relies on the following two lemmas. Lemma 1 shows the decrease of the objective function values for the sequence generated by the EM algorithm (10). By switching u and h, we can show that $Q(u, h^{k+1}) \leq Q(u, h^k)$ for any u. For a fixed h, Lemma 2 guarantees the FOTV-regularized objective function decreases with respect to u. Therefore, we have

$$Q(u^{k+1}, h^{k+1}) \leq Q(u^k, h^{k+1}) \leq Q(u^k, h^k).$$

It is obvious that the objective function $Q(u,h) \geq 0$. Then it follows from the Bolzano–Weierstrass Theorem that there exists a convergent subsequence.

For the notational convenience, we assume u, h are column vectors, define a matrix H such that $Hu := h\circ u$, and denote $(Hu)_i$ as the ith element of Hu. Therefore, we can rewrite the EM update (10) as

$$u_j^{k+1} = \frac{u_j^k}{\sum_i H_{ij}}\sum_i \frac{H_{ij}f_j}{(Hu^k)_i}. \tag{46}$$

Lemma 1 *Given f and H, define*

$$F(u) := \sum_i \Big((Hu)_i - f_i\log(Hu)_i\Big) \tag{47}$$

For the sequence generated by (46), we have $F(u^{k+1}) \leq F(u^k)$.

Proof The proof follows the majorize-minimization (MM) framework [32,41]. In particular, we define a surrogate function of F, denoted by $G(u, u^k)$, which satisfies the following two conditions:

$$\begin{aligned} &F(u^k) = G(u^k, u^k)\\ &F(u) \leq G(u, u^k), \quad \forall u. \end{aligned} \tag{48}$$

If $u^{k+1} = \operatorname{argmin}_u G(u, u^k)$, then

$$F(u^{k+1}) \leq G(u^{k+1}, u^k) \leq G(u^k, u^k) = F(u^k),$$

where the first inequality and the last equality are by definition in (48), and the second inequality is because that u^{k+1} minimizes $G(u, u^k)$.

We consider

$$G(u, u^k) = \sum_i (Hu)_i - \sum_i f_i \sum_j \frac{H_{ij}u_j^k}{(Hu^k)_i}\log\left(\frac{H_{ij}u_j}{\frac{H_{ij}u_j^k}{(Hu^k)_i}}\right). \tag{49}$$

We will show G is a surrogate function for F and the EM update (46) minimizes $G(u, u^k)$.

Author's personal copy

Simple calculations lead to $G(u^k, u^k) = F(u^k)$. To show $F(u) \leq G(u, u^k)$, we define $a_{ij} = \frac{H_{ij}u_j^k}{(Hu^k)_i}$. It is straightforward that $a_{ij} \geq 0$ and $\sum_j a_{ij} = 1,\ \forall i$. Then by Jensen's inequality, we have $\forall i$,

$$\sum_j \frac{H_{ij}u_j^k}{(Hu^k)_i}\log\left(\frac{H_{ij}u_j}{\frac{H_{ij}u_j^k}{(Hu^k)_i}}\right) = \sum_j a_{ij}\log\left(\frac{H_{ij}u_j}{a_{ij}}\right) \leq \log\Big(\sum_j H_{ij}u_j\Big). \tag{50}$$

Therefore, by definitions in (49) and (47), we have $F(u) \leq G(u, u^k)$, and hence, G is a surrogate function of F.

To show that the EM update (46) minimizes $G(u, u^k)$, we take the gradient of $G(u, u^k)$ with respect to u and set equal to zero, thus leading to

$$\sum_i H_{ij} - \frac{\sum_i f_i a_{ij}}{u_j} = 0. \tag{51}$$

Therefore, we get

$$u_j = \frac{\sum_i f_i a_{ij}}{\sum_i H_{ij}} = \frac{u_j^k}{\sum_i H_{ij}}\sum_i \frac{H_{ij}f_j}{(Hu^k)_i}, \tag{52}$$

which is equivalent to (46). By the MM framework, we have $F(u^{k+1}) \leq F(u^k)$. □

Lemma 2 *Define an FOTV regularized objective function*

$$E(u) := \|\nabla^\alpha u\|_1 + \beta\sum_i (Hu)_i - f_i\log((Hu)_i), \tag{53}$$

and consider the following iterative scheme

$$u^{k+1} = \operatorname{argmin}_u \|\nabla^\alpha u\|_1 + \beta\sum_j\Big(\sum_i H_{ij}\Big)\big(u_j - u_j^{k+\frac{1}{2}}\log u_j\big), \tag{54}$$

with $u^{k+\frac{1}{2}}$ defined by (46). We can show that $E(u^{k+1}) \leq E(u^k)$.

Proof Denote $R(u) = \|\nabla^\alpha u\|_1$. Since u^{k+1} is the optimal solution for (54), we have

$$R(u^{k+1}) + \beta\sum_j\Big(\sum_i H_{ij}\Big)\big(u_j^{k+1} - u_j^{k+\frac{1}{2}}\log u_j^{k+1}\big) \leq R(u^k) + \beta\sum_j\Big(\sum_i H_{ij}\Big)\big(u_j^k - u_j^{k+\frac{1}{2}}\log u_j^k\big),$$

which implies that

$$\begin{aligned} R(u^{k+1}) - R(u^k) &\leq \beta\sum_j\Big(\sum_i H_{ij}\Big)\left(u_j^k - u_j^{k+1} + u_j^{k+\frac{1}{2}}\log\frac{u_j^{k+1}}{u_j^k}\right) \\ &= \beta\Big(\sum_i\big((Hu^k)_i - (Hu^{k+1})_i\big) \\ &\quad + \sum_j\Big(\sum_i H_{ij}\Big)u_j^{k+\frac{1}{2}}\log\frac{u_j^{k+1}}{u_j^k}\Big). \end{aligned} \tag{55}$$

Using the definition of (46) and the inequality (55), we can compute

$$\begin{aligned} &\frac{1}{\beta}\big(E(u^{k+1}) - E(u^k)\big) \\ &\leq \sum_i f_i\log\left(\frac{(Hu^k)_i}{(Hu^{k+1})_i}\right) + \sum_{ij} f_i a_{ij}\log\frac{u_j^{k+1}}{u_j^k} \\ &\leq \sum_i f_i\log\left(\frac{(Hu^k)_i}{(Hu^{k+1})_i}\right) + \sum_i f_i\log\left(\sum_j a_{ij}\frac{u_j^{k+1}}{u_j^k}\right), \end{aligned} \tag{56}$$

where the last inequality is from Jensen's inequality and $a_{ij} = \frac{H_{ij}u_j^k}{(Hu^k)_i}$. Simple calculations show that

$$\sum_j a_{ij}\frac{u_j^{k+1}}{u_j^k} = \sum_j \frac{H_{ij}u_j^{k+1}}{(Hu^k)_i} = \frac{(Hu^{k+1})_i}{(Hu^k)_i}. \tag{57}$$

Since $f_i \geq 0$, we get $E(u^{k+1}) - E(u^k) \leq 0$ by plugging (57) into (56). □

References

1. Aljadaany, R., Pal, D.K., Savvides, M.: Douglas–Rachford networks: learning both the image prior and data fidelity terms for blind image deconvolution. In: IEEE Conference on Computer Vision and Pattern Recognition (2019)
2. Almeida, M.S., Figueiredo, M.: Deconvolving images with unknown boundaries using the alternating direction method of multipliers. IEEE Trans. Image process. **22**(8), 3074–3086 (2013)
3. Azzari, L., Foi, A.: Variance stabilization in Poisson image deblurring. In: IEEE International Symposium on Biomedical Imaging (ISBI), pp. 728–731. IEEE (2017)
4. Babacan, S.D., Molina, R., Katsaggelos, A.K.: Variational Bayesian blind deconvolution using a total variation prior. IEEE Trans. Image Process. **18**(1), 12–26 (2008)
5. Bahmani, S., Romberg, J.: Lifting for blind deconvolution in random mask imaging: identifiability and convex relaxation. SIAM J. Imaging Sci. **8**(4), 2203–2238 (2015)
6. Bajić, B., Lindblad, J., Sladoje, N.: Blind restoration of images degraded with mixed Poisson–Gaussian noise with application in

Author's personal copy

transmission electron microscopy. In: International Symposium on Biomedical Imaging, pp. 123–127. IEEE (2016)
7. Beck, A., Teboulle, M.: Fast gradient-based algorithms for constrained total variation image denoising and deblurring problems. IEEE Trans. Image Process. **18**(11), 2419–2434 (2009)
8. Bertero, M., Boccacci, P., Desiderà, G., Vicidomini, G.: Image deblurring with Poisson data: from cells to galaxies. Inverse Probl. **25**(12), 123006 (2009)
9. Biggs, D.S., Andrews, M.: Acceleration of iterative image restoration algorithms. Appl. Opt. **36**(8), 1766–1775 (1997)
10. Boyd, S., Parikh, N., Chu, E., Peleato, B., Eckstein, J.: Distributed optimization and statistical learning via the alternating direction method of multipliers. Found. Trends Mach. Learn. **3**(1), 1–122 (2011)
11. Candès, E.J., Strohmer, T., Voroninski, V.: Phaselift: exact and stable signal recovery from magnitude measurements via convex programming. Commun. Pure Appl. Math. **66**(8), 1241–1274 (2013)
12. Carasso, A.S.: Direct blind deconvolution. SIAM J. Appl. Math. **61**(6), 1980–2007 (2001)
13. Chambolle, A., Pock, T.: An introduction to continuous optimization for imaging. Acta Numer. **25**, 161–319 (2016)
14. Chan, R.H., Chan, T.F., Wong, C.: Cosine transform based preconditioners for total variation deblurring. IEEE Trans. Image Process. **8**(10), 1472–1478 (1999)
15. Chan, R.H., Tao, M., Yuan, X.: Constrained total variation deblurring models and fast algorithms based on alternating direction method of multipliers. SIAM J. Imaging Sci. **6**(1), 680–697 (2013)
16. Chan, T.F., Wong, C.: Total variation blind deconvolution. IEEE Trans. Image Process. **7**(3), 370–375 (1998)
17. Cho, S., Lee, S.: Fast motion deblurring. In: ACM SIGGRAPH Asia 2009 Papers, pp. 1–8 (2009)
18. Chowdhury, M.R., Zhang, J., Qin, J., Lou, Y.: Poisson image denoising based on fractional-order total variation. Inverse Probl. Imaging **14**(1), 77 (2020)
19. Dempster, A.P., Laird, N.M., Rubin, D.B.: Maximum likelihood from incomplete data via the EM algorithm. J. R. Stat. Soc. Ser. B (Methodol.) **39**(1), 1–22 (1977)
20. Dey, N., Blanc-Feraud, L., Zimmer, C., Roux, P., Kam, Z., Olivo-Marin, J., Zerubia, J.: Richardson–Lucy algorithm with total variation regularization for 3D confocal microscope deconvolution. Microsoft Res. Technol. **69**(4), 260–266 (2006)
21. Donatelli, M., Estatico, C., Martinelli, A., Serra-Capizzano, S.: Improved image deblurring with anti-reflective boundary conditions and re-blurring. Inverse Probl. **22**(6), 2035 (2006)
22. Dupé, F.X., Fadili, M.J., Starck, J.L.: Image deconvolution under Poisson noise using sparse representations and proximal thresholding iteration. In: International Conference on Acquisition , Speech Signal Process, pp. 761–764. IEEE (2008)
23. Fergus, R., Singh, B., Hertzmann, A., Roweis, S.T., Freeman, W.T.: Removing camera shake from a single photograph. In: ACM Transactions on Graphics, vol. 25, pp. 787–794. ACM (2006)
24. Figueiredo, M., Bioucas-Dias, J.: Restoration of Poissonian images using alternating direction optimization. IEEE Trans. Image Process. **19**(12), 3133–3145 (2010)
25. Fish, D., Brinicombe, A., Pike, E., Walker, J.: Blind deconvolution by means of the Richardson–Lucy algorithm. J. Opt. Soc. Am. A **12**(1), 58–65 (1995)
26. Gabay, D., Mercier, B.: A dual algorithm for the solution of nonlinear variational problems via finite element approximation. Comput. Math. Appl. **2**(1), 17–40 (1976)
27. Glowinski, R., Marroco, A.: Sur l'approximation, par éléments finis d'ordre un, et la résolution, par pénalisation-dualité d'une classe de problèmes de dirichlet non linéaires. ESAIM Math. Model. Numer. Anal. **9**(R2), 41–76 (1975)
28. Hansen, P.C., Nagy, J., O'leary, D.P.: Deblurring Images: Matrices, Spectra, and Filtering, vol. 3. SIAM, Philadelphia (2006)
29. He, T., Hu, J., Huang, H.: Hybrid high-order nonlocal gradient sparsity regularization for Poisson image deconvolution. Appl. Opt. **57**(35), 10243–10256 (2018)
30. Huang, J., Huang, T.Z.: A nonstationary accelerating alternating direction method for frame-based Poissonian image deblurring. J. Comput. Appl. Math. **352**, 181–193 (2019)
31. Hunt, B.R.: The application of constrained least squares estimation to image restoration by digital computer. IEEE Trans. Comput. **100**(9), 805–812 (1973)
32. Hunter, D.R., Lange, K.: A tutorial on MM algorithms. Am. Stat. **58**(1), 30–37 (2004)
33. Jin, M., Roth, S., Favaro, P.: Normalized blind deconvolution. In: Proceedings of the European Conference on Computer Vision, pp. 668–684 (2018)
34. Karush, W.: Minima of functions of several variables with inequalities as side constraints. M.Sc. Dissertation. Department of Mathematics, University of Chicago (1939)
35. Krishnan, D., Tay, T., Fergus, R.: Blind deconvolution using a normalized sparsity measure. In: IEEE Conference on Computer Vision and Pattern Recognition, pp. 233–240. IEEE (2011)
36. Kuhn, H.W., Tucker, A.W.: Nonlinear programming. In: Neyman, E. (ed.) Berkeley Symposium on Mathematics of Stats and Probability, pp. 481–492. University of California Press, Berkeley (1951)
37. Kundur, D., Hatzinakos, D.: Blind image deconvolution. IEEE Signal Process. Mag. **13**(3), 43–64 (1996)
38. Kupyn, O., Budzan, V., Mykhailych, M., Mishkin, D., Matas, J.: Deblurgan: Blind motion deblurring using conditional adversarial networks. In: Proceedings of the IEEE Conference on Computer Vision and Pattern Recognition, pp. 8183–8192 (2018)
39. Lai, W., Huang, J., Hu, Z., Ahuja, N., Yang, M.: A comparative study for single image blind deblurring. In: IEEE Conference on Computer Vision and Pattern Recognition, pp. 1701–1709 (2016)
40. Landi, G., Piccolomini, E.L.: An efficient method for nonnegatively constrained total variation-based denoising of medical images corrupted by Poisson noise. Comput. Med. Imaging Graph. **36**(1), 38–46 (2012)
41. Lange, K.: MM Optimization Algorithms, vol. 147. SIAM, Philadelphia (2016)
42. Le, T., Chartrand, R., Asaki, T.J.: A variational approach to reconstructing images corrupted by Poisson noise. J. Math. Imaging Vis. **27**(3), 257–263 (2007)
43. Levin, A., Weiss, Y., Durand, F., Freeman, W.T.: Efficient marginal likelihood optimization in blind deconvolution. In: IEEE Conference on Computer Vision and Pattern Recognition, pp. 2657–2664 (2011)
44. Levin, A., Weiss, Y., Durand, F., Freeman, W.T.: Understanding blind deconvolution algorithms. IEEE Trans. Pattern Anal. Mach. Intell. **33**(12), 2354–2367 (2011)
45. Li, L., Pan, J., Lai, W.S., Gao, C., Sang, N., Yang, M.H.: Blind image deblurring via deep discriminative priors. Int. J. Comput. Vis. **127**(8), 1025–1043 (2019)
46. Li, S., Tang, G., Wakin, M.B.: Simultaneous blind deconvolution and phase retrieval with tensor iterative hard thresholding. In: International Conference on Acoustics, Speech, and Signal Processing, pp. 2977–2981. IEEE (2019)
47. Liu, H., Gu, J., Huang, C.: Image deblurring by generalized total variation regularization and least squares fidelity. In: International Conference on Information and Automation, pp. 1945–1949. IEEE (2016)
48. Ljubenović, M., Figueiredo, M.A.: Blind image deblurring using class-adapted image priors. In: IEEE International Conference on Image Processing (ICIP), pp. 490–494 (2017)
49. Lou, Y., Zhang, X., Osher, S.J., Bertozzi, A.L.: Image recovery via nonlocal operators. J. Sci. Comput. **42**(2), 185–197 (2010)

Author's personal copy

50. Lucy, L.B.: An iterative technique for the rectification of observed distributions. Astrophys. J. **79**, 745 (1974)
51. Ma, L., Moisan, L., Yu, J., Zeng, T.: A dictionary learning approach for Poisson image deblurring. IEEE Trans. Med. Imaging **32**(7), 1277–1289 (2013)
52. McCallum, B.C.: Blind deconvolution by simulated annealing. Opt. Commun. **75**(2), 101–105 (1990)
53. Perrone, D., Favaro, P.: A clearer picture of total variation blind deconvolution. IEEE Trans. Pattern Anal. Mach. Intell. **38**(6), 1041–1055 (2015)
54. Prato, M., La Camera, A., Bonettini, S.: An alternating minimization method for blind deconvolution from poisson data. In: Journal of Physics: Conference Series, vol. 542, p. 012006. IOP Publishing (2014)
55. Qin, J., Yi, X., Weiss, S.: A novel fluorescence microscopy image deconvolution approach. In: IEEE Intrnational Symposium Biomedical Imaging, pp. 441–444 (2018)
56. Qin, J., Yi, X., Weiss, S., Osher, S.: Shearlet-TGV based fluorescence microscopy image deconvolution. UCLA CAM Report (14-32) (2014)
57. Richardson, W.H.: Bayesian-based iterative method of image restoration. J. Opt. Soc. Am. A **62**(1), 55–59 (1972)
58. Rudin, L., Osher, S., Fatemi, E.: Nonlinear total variation based noise removal algorithms. Physica D **60**, 259–268 (1992)
59. Ruiz, P., Zhou, X., Mateos, J., Molina, R., Katsaggelos, A.K.: Variational Bayesian blind image deconvolution: A review. Dig. Sig. Process. **47**, 116–127 (2015)
60. Sawatzky, A., Brune, C., Kosters, T., Wubbeling, F., Burger, M.: EM-TV methods for inverse problems with Poisson noise. Level Set and PDE Based Reconstruction Methods in Imaging, Lecture Notes in Mathematics (2090), pp. 71–142 (2013)
61. Schuler, C.J., Hirsch, M., Harmeling, S., Schölkopf, B.: Learning to deblur. IEEE Trans. Pattern Anal. Mach. Intell. **38**(7), 1439–1451 (2015)
62. Setzer, S., Steidl, G., Teuber, T.: Deblurring Poissonian images by split Bregman techniques. J. Vis. Commun. Image R. **21**(3), 193–199 (2010)
63. Shan, Q., Jia, J., Agarwala, A.: High-quality motion deblurring from a single image. ACM Trans. Graph. **27**(3), 73 (2008)
64. Shepp, L.A., Vardi, Y.: Maximum likelihood reconstruction for emission tomography. IEEE Trans. Med. Imaging **1**(2), 113–122 (1982)
65. Sun, J., Cao, W., Xu, Z., Ponce, J.: Learning a convolutional neural network for non-uniform motion blur removal. In: Proceedings of the IEEE Conference on Computer Vision Pattern Recognition, pp. 769–777 (2015)
66. Tikhonov, A.N., Goncharsky, A.V., Stepanov, V., Yagola, A.G.: Numerical Methods for the Solution of Ill-Posed Problems, vol. 328. Springer, Berlin (2013)
67. Vono, M., Dobigeon, N., Chainais, P.: Bayesian image restoration under Poisson noise and log-concave prior. In: International Conference on Acoustics, Speech, and Signal Processing, pp. 1712–1716. IEEE (2019)
68. Wang, Z., Bovik, A.C., Sheikh, H.R., Simoncelli, E.P.: Image quality assessment: from error visibility to structural similarity. IEEE Trans. Image Process. **13**(4), 600–612 (2004)
69. Xu, J., Chang, H.B., Qin, J.: Domain decomposition method for image deblurring. J. Comput. Appl. Math. **271**, 401–414 (2014)
70. Xu, L., Jia, J.: Two-phase kernel estimation for robust motion deblurring. In: European Conference on Computer Vision, pp. 157–170. Springer (2010)
71. Yan, M., Chen, J., Vese, L.A., Villasenor, J., Bui, A., Cong, J.: EM + TV based reconstruction for cone-beam ct with reduced radiation. In: International Symposium on Visual Computing, pp. 1–10. Springer (2011)
72. You, Y., Kaveh, M.: A regularization approach to joint blur identification and image restoration. IEEE Trans. Image Process. **5**(3), 416–428 (1996)
73. You, Y., Kaveh, M.: Blind image restoration by anisotropic regularization. IEEE Trans. Image Process. **8**(3), 396–407 (1999)
74. Zhang, J., Wei, Z., Xiao, L.: Adaptive fractional-order multi-scale method for image denoising. J. Math. Imaging Vis. **43**(1), 39–49 (2012)
75. Zhou, L., Tang, J.: Fraction-order total variation blind image restoration based on l1-norm. Appl. Math. Model. **51**, 469–476 (2017)

Publisher's Note Springer Nature remains neutral with regard to jurisdictional claims in published maps and institutional affiliations.

Mujibur Rahman Chowdhury received a B.Sc. and M.S. degree in Mathematics from the University of Chittagong, Bangladesh, in 2009 and 2010. He also received an M.S. degree in Mathematics, an M.S. degree in Data Science (with Mathematics) from Lamar University and UT Dallas, USA, in 2015 and 2019. He obtained his Ph.D. in Mathematics from the University of Texas at Dallas, USA, in 2020. His research interests are mathematical image processing, medical imaging, and machine learning. His current research focused on image denoising, deconvolution, and CT reconstruction.

Jing Qin is an assistant professor in the Department of Mathematics, University of Kentucky at Lexington, KY. She received her B.S. degree in mathematics from Xuzhou Normal University, Jiangsu, China, in 2005, her M.S. degree in mathematics from East China Normal University, Shanghai, China, in 2008, and her Ph.D. in applied mathematics from Case Western Reserve University, Cleveland, OH, in 2013. From 2013 to 2016, she was an assistant adjunct professor in the Department of Mathematics at the University of California at Los Angeles. From 2016 to 2019, she worked as an assistant professor in the Department of Mathematical Sciences, Montana State University, Bozeman, MT. Her research interests include mathematical image processing, numerical optimization and high-dimensional data analysis.

Author's personal copy

Yifei Lou has been an Assistant Professor in the Mathematical Sciences Department, University of Texas Dallas, since 2014. She received her Ph.D. in Applied Math from the University of California Los Angeles (UCLA) in 2010. After graduation, she was a postdoctoral fellow at the School of Electrical and Computer Engineering Georgia Institute of Technology, followed by another postdoc training at the Department of Mathematics, University of California Irvine from 2012 to 2014. Dr. Lou received the National Science Foundation CAREER Award in 2019. Her research interests include compressive sensing and its applications, image analysis (medical imaging, hyperspectral, imaging through turbulence), and (nonconvex) optimization algorithms.